



# Validation and time step determination of discrete element modeling of flexible fibers



Y. Guo<sup>a,\*</sup>, C. Wassgren<sup>b</sup>, B. Hancock<sup>c</sup>, W. Ketterhagen<sup>c</sup>, J. Curtis<sup>a</sup>

<sup>a</sup> Chemical Engineering Department, University of Florida, Gainesville, FL 32611, United States

<sup>b</sup> School of Mechanical Engineering, Purdue University, West Lafayette, IN 47907, United States

<sup>c</sup> Pfizer, Inc., Groton, CT 06340, United States

## ARTICLE INFO

### Article history:

Received 23 April 2013

Received in revised form 25 August 2013

Accepted 1 September 2013

Available online 14 September 2013

### Keywords:

Flexible fiber

Discrete Element Method

Validation

Time step

## ABSTRACT

In this paper, a flexible fiber model, based on the Discrete Element Method (DEM) and the bonded-particle model by Potyondy and Cundall (*International Journal of Rock Mechanics & Mining Sciences* 41 (2004) 1329–1364), is comprehensively examined by considering the cases of the bending, stretching, and twisting of a fiber under static loads and dynamic vibrations. The numerical simulation results are in good agreement with the analytical predictions from elastic thin beam theories. In addition, a time step criterion is discussed and proposed in order to ensure numerical stability and obtain correct dynamic behaviors of fibers. It is found that the time step should be less than the time it takes for an axial extensional/compressional wave to travel a single bond length.

© 2013 Elsevier B.V. All rights reserved.

## 1. Introduction

Flexible, rod-like particles and filamentous fibers play an important role in industries and nature. For example, flexible chemical and natural fibers are critical raw materials in the manufacture of fabrics, fiber-reinforced composites, cables, biomass fuels, tobacco, and paper [1–10]. The properties of these products depend on the fiber orientation, spatial distribution, and network formation. Therefore, understanding dynamics and rheology of fibers and fiber suspensions is essential for optimizing manufacturing procedures and improving product quality. For biological systems, understanding dynamic behavior of flexible biopolymer chains (e.g., F-actin, wormlike micelles, and neurofilaments) is important for revealing biological and physical mechanisms [11]. Recently, flexible ceramic nanofibers have been produced and applied to tissue engineering, filtration, and catalyst support [12]. Thus, flexible fibers have been attracting significant research interest due to their traditional and new applications.

As an effective complement to experimental studies, computational simulations have been widely used to study the dynamics of fibers and fiber suspensions [1–11] due to the ease with which particle scale information may be accessed, such as the deformation of particles and the development of fiber flocs, which may be difficult to obtain from the experiments. In various numerical models, flexible fibers are usually represented by chains of spheres [1–4,11], chains of prolate spheroids [5], or chains of cylindrical short rods [6–10], which are connected by elastic bonds or ball-socket joints. The dynamics of a fiber are modeled

by tracking the motion of each segment (i.e., sphere, spheroid, or rod) under internal interactions with the neighboring segments through bonds or ball-socket joints, and external forces, such as hydraulic forces, contact forces with other fibers, and gravitational forces.

In the completely flexible fiber model [3], a fiber can bend and twist freely without any bending and torsional restoring moments, and only the axial stretching/compressing deformations are restrained by linear springs. In the partially-flexible fiber models [1,2,4–11], bending and twisting deformations of two connected segments or bonds are described using linear elastic models. The bending/torsional restoring moments acting on the segments are linearly proportional to their relative bending/torsional angular displacements through the corresponding stiffness constants, which can be expressed as functions of the Young's modulus, shear modulus, and cross sectional properties (area and area moment of inertia) of the fiber.

Different methods have been used to calculate the interaction forces between the neighboring segments which are connected through the bonds or joints. In the rod-chain models [5,7–10] and the sphere-chain model by Qi [11], the axial extension/compression is ignored. Therefore, the lengths of bonds or the distances between two successive joints remain constant during the fiber deformation process. In addition, the connectivity of two segments in a fiber chain is ensured by imposing the “no-slip” condition that the relative velocity between them at the joint is zero. Thus, a set of constraining equations can be established based on the “no axial deformation” condition and the “no-slip” condition, and the interaction forces between each pair of connected segments can be obtained by solving this set of equations.

In the sphere-chain model [1–4] and the rod-chain model [6], the axial extension/compression is modeled as following a linear spring

\* Corresponding author.

E-mail address: [guoyu03@gmail.com](mailto:guoyu03@gmail.com) (Y. Guo).

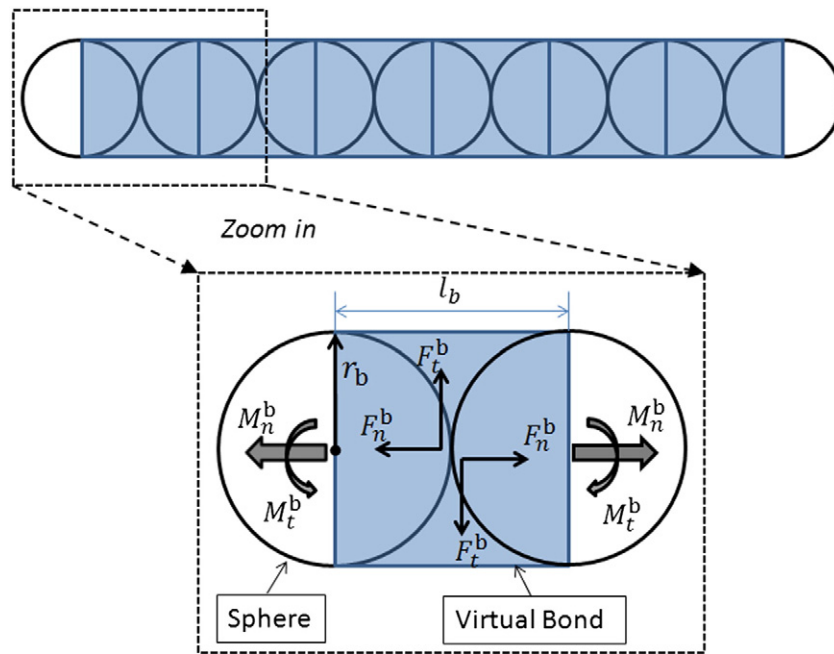


Fig. 1. Illustration of the bonded rod-like particle model.

behavior which has the normal force (in the major axis direction of bond or rod) proportional to the change in bond length or the distance between two successive joints. However, different methods are used to determine the tangential force (which is perpendicular to the major axis direction of bond or rod). In the models by Yamamoto and Matsuoka [1] and Kabanemi and Hétu [2], the tangential forces are obtained by imposing the “no-slip” conditions at the contact points for the neighboring spheres in a chain. While in the model by Nguyen et al. [4], the Euler-Bernoulli beam theory is employed to describe the bending deformation of a bond, and the tangential forces acting on the bonded spheres are determined by the angular orientations of the two spheres relative to the major axis direction of the bond between the spheres. In the model by Ning and Melrose [6], the tangential forces are determined by the bending moments and the bond orientations based on the force/moment balance equations on the bond.

Efforts have been made to validate these flexible fiber models by comparing the simulation results of sheared fiber suspensions with well-established theories and experimental results [1,2,5,8–11]. Nguyen et al. [4] and Ning and Melrose [6] examined bending behavior of a single flexible rod under static loads and dynamic vibrations. In their work, good agreement was obtained between the simulation results and elastic beam theories for the deflection of the free end of the rod.

In the present work, a flexible fiber model, based on the bonded sphere model proposed by Potyondy and Cundall [13], is comprehensively validated by testing the mechanical behavior of a single fiber. The bonded sphere model was originally developed to investigate the fracture of rocks under external loads [13], and was recently applied to study the removal and separation of grape berries from the multi-branch stems [14], which were modeled by several connected, flexible fibers. The major features of the present fiber model and the differences between this work and previous studies [1–11] are summarized as follows:

- i. In the present fiber model, the bond normal force, bending moment, and torsional moment are determined using similar linear models as in [1]. However, the tangential force is simply calculated from the shear strain between the cross sections of the bond. This method of determining the interaction forces between two paired segments is easier to implement and may be more economic computationally compared to those adopted in [1,2,5,7–11], in which the constraining

conditions are imposed at the joints or contact points and a set of equations need to be solved.

- ii. The present fiber model is a bonded-sphere model. Compared to the cylindrical rod-chain models [5–10], the bonded-sphere model has several advantages: (a) In case of a dense system where fiber–fiber contacts are frequent, the contacts between the segments from different fibers have to be considered. Under this condition, the occurrence of contact and the size of the overlap (used to calculate the contact force) are much easier to determine for the sphere–sphere contact than the cylinder–cylinder contact due to the geometric simplicity of spheres; (b) It is easier and more economic to compute the three-dimensional rotation of spheres than cylinders. However, the bonded-sphere model has the drawback that a fiber formed by spheres has a bumpy surface, while commonly-encountered fibers have smooth, cylindrical surfaces. Nevertheless, the roughness of the surface of a bonded-sphere fiber can be reduced by using more constituent spheres and allowing larger overlaps between the neighboring spheres, but the computational cost will be increased due to the increase in the number of spheres and bonds.
- iii. Previous fiber model validation studies [4,6] examined the deflection of the free end of a fiber cantilever which bent under static loads and dynamic vibrations. However, in this study, besides the free end, the distribution of deflection over the whole fiber is checked. In addition, the distributions of shear force and bending moment over the fiber are also examined. The examination of these distributions provides a full check on the mechanical behavior of the whole fiber. Furthermore, correct modeling of distributions of bonding forces and moments is important because this information can provide accurate predictions of the critical positions where the maximum stresses occur and failure/breakage can possibly initiate.
- iv. Previous studies [4,6] verified fiber bending only, while this paper presents a comprehensive examination of fiber bending, stretching/compressing, and twisting.
- v. In this work, a criterion for the determination of an appropriate simulation integration time step is proposed to ensure numerical stability and obtain the correct dynamic behavior of fibers.

This paper is organized as follows: a brief description of the flexible fiber model is presented in Section 2; the fiber bending, stretching, and twisting are verified in Sections 3, 4 and 5, respectively; the time step

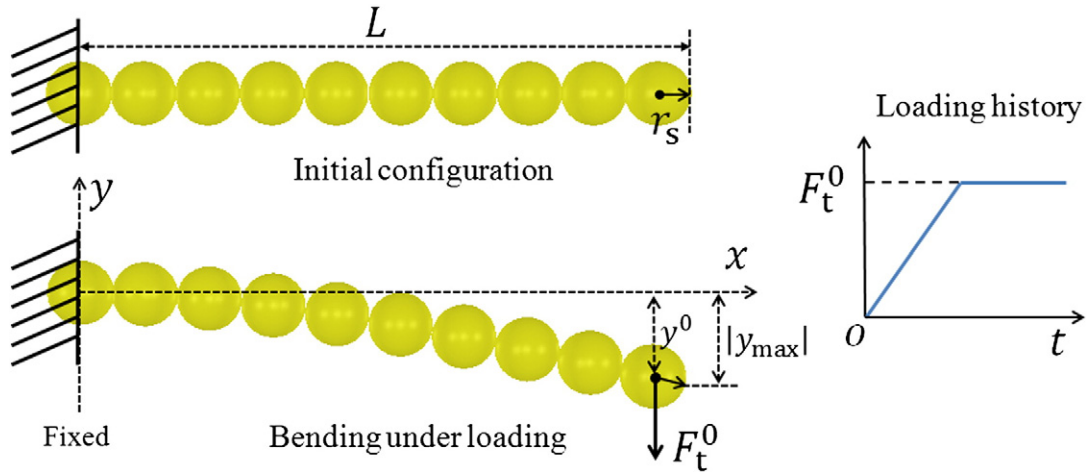


Fig. 2. Bending of a fiber formed by bonding spheres.

criterion for the modeling of fiber dynamics is proposed in Section 6, and the paper is concluded in Section 7.

## 2. Flexible fiber model

In the present work, a fiber is modeled by connecting a number of identical spheres in a straight line using elastic bonds, as shown in

Fig. 1. Two ends of a single bond are fixed on the centers of two neighboring spheres, respectively, and translate/rotate with the spheres. Thus, the relative movement of the constituent spheres in a composite particle leads to the deformation of the bonds and also the particle. In response, bond forces/moments are induced and exerted on the spheres to resist the deformation. According to the bonded-particle model [13], the bond forces/moments can be calculated using an incremental method as follows:

$$dF_n^b = \frac{EA}{l_b} d\delta_n^r = \frac{EA}{l_b} v_n^r dt, \quad (1)$$

$$dF_t^b = \frac{GA}{l_b} d\delta_t^r = \frac{GA}{l_b} v_t^r dt, \quad (2)$$

$$dM_n^b = \frac{GI_p}{l_b} d\theta_n^r = \frac{GI_p}{l_b} \dot{\theta}_n^r dt, \quad (3)$$

and,

$$dM_t^b = \frac{EI}{l_b} d\theta_t^r = \frac{EI}{l_b} \dot{\theta}_t^r dt, \quad (4)$$

in which  $dF_n^b$ ,  $dF_t^b$ ,  $dM_n^b$ , and  $dM_t^b$  are the incremental normal force  $F_n^b$ , shear force  $F_t^b$ , torsional moment  $M_n^b$ , and bending moment  $M_t^b$ , respectively, and  $d\delta_n^r$ ,  $d\delta_t^r$ ,  $d\theta_n^r$ , and  $d\theta_t^r$  are the incremental relative normal displacement  $\delta_n^r$ , tangential displacement  $\delta_t^r$ , torsional angular displacement  $\theta_n^r$ , and bending angular displacement  $\theta_t^r$ , respectively. The cylindrical bond has a radius  $r_b$ , length  $l_b$ , cross sectional area  $A = \pi r_b^2$ , area moment of inertia  $I = \pi r_b^4/4$ , and polar area moment of inertia  $I_p = \pi r_b^4/2$ . The bond Young's modulus  $E$  and shear modulus  $G$  are related by the Poisson's ratio  $\xi$ :  $G = \frac{E}{2(1+\xi)}$ . The incremental relative displacements can be calculated based on the corresponding relative velocities ( $v_n^r$ ,  $v_t^r$ ,  $\dot{\theta}_n^r$ , and  $\dot{\theta}_t^r$ ) and the time step  $dt$ .

The motions of individual spheres in each fiber are governed by Newton's second law of motion, i.e.,

$$m_s \frac{d^2 \mathbf{x}_s}{dt^2} = \mathbf{F}^b + \mathbf{F}^c + \mathbf{F}^h + m_s \mathbf{g}, \quad (5)$$

and,

$$J_s \frac{d^2 \theta_s}{dt^2} = \mathbf{M}^b + \mathbf{M}^c, \quad (6)$$

in which  $\mathbf{x}_s$  and  $\theta_s$  are the translational displacement and angular displacement, respectively, of the sphere of mass  $m_s$  and moment of inertia

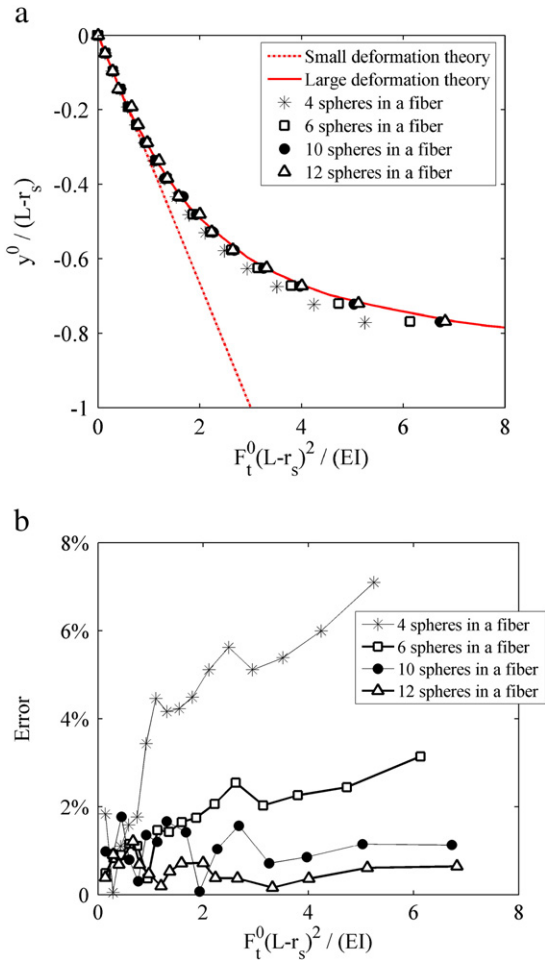


Fig. 3. Normalized deflection of the sphere center at the free end of the cantilever (a) and the errors in the simulation results compared to large deformation theory (b) as a function of normalized loading in case of fiber bending.

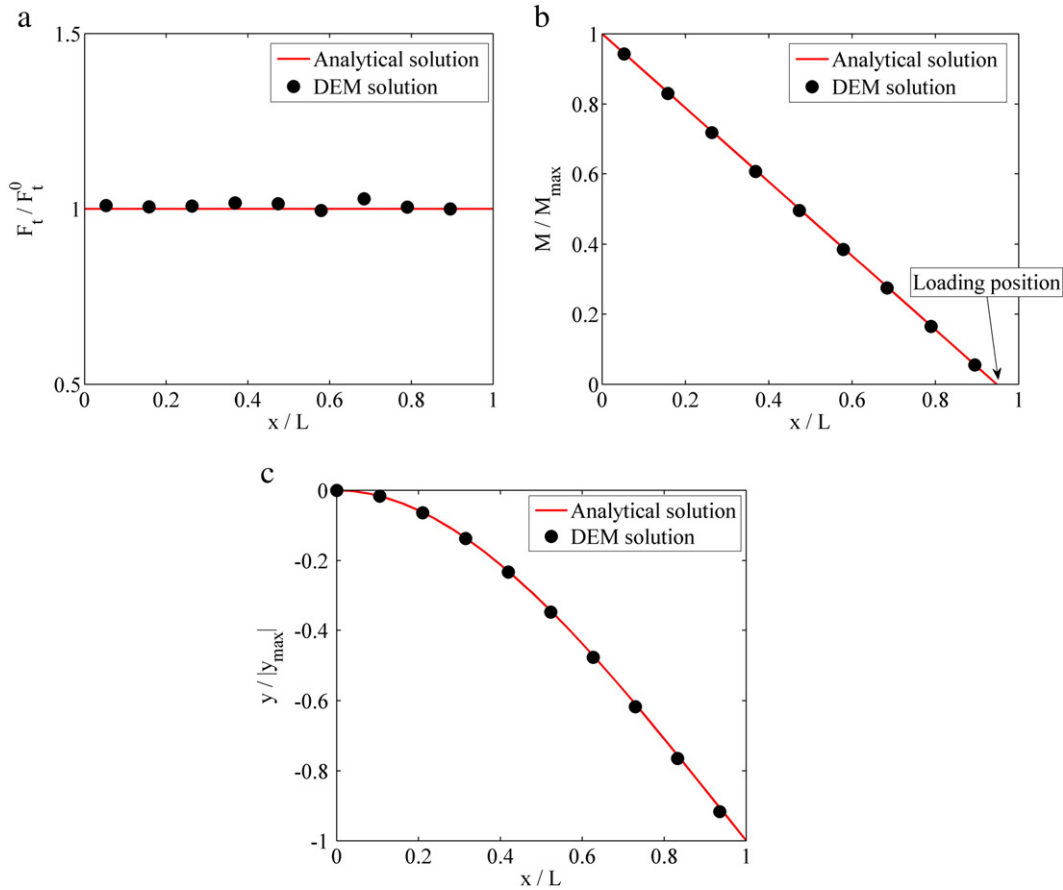


Fig. 4. Distributions of tangential force (a), bending moment (b), and deflection (c) along the x-axis in case of fiber bending deformation.

$J_s$ . The translational motion of a sphere is driven by a number of forces:  $\mathbf{F}^b$  represents the bonding force;  $\mathbf{F}^c$  is the force due to contacts with the spheres which are from the same fiber but not bonded with it or from different fibers (no contact force exists between two bonded spheres in a fiber even if there is an overlap under the axial compression), and the contact force  $\mathbf{F}^c$  can be determined using the Hertz–Mindlin–Deresiewicz theory [15];  $\mathbf{F}^h$  is a hydraulic force if the fiber is immersed in a fluid; and  $m_s \mathbf{g}$  represents the gravitational force. The rotation of the sphere is driven by  $\mathbf{M}^b$ , which arises from the bond shear forces and bond bending/torsional moments, and  $\mathbf{M}^c$  arising from the contact force  $\mathbf{F}^c$ .

The resultant mechanical behavior of a fiber can be treated as the superposition of the behavior under each external force, and the resultant deformation can be decomposed into three basic deformations: bending, axial stretching/compressing, and twisting. Therefore, the complex behavior of a fiber under various external force conditions may be validated by examining the three basic deformations separately. In the current model, the contact force  $\mathbf{F}^c$ , hydraulic force  $\mathbf{F}^h$ , gravitational force  $m_s \mathbf{g}$ , and moment  $\mathbf{M}^c$  are assumed to be absent, and an external force/torque is applied to the free end of a fiber to make the fiber bend, stretch/compress, or twist.

### 3. Fiber bending

Cantilever bending of a flexible fiber formed by bonding spheres is simulated, as shown in Fig. 2. The sphere at one end of the bonded particle is fixed, and a point load perpendicular to the axis of the fiber is applied to the center of the sphere at the other end. The quasi-static loading process is achieved by increasing the load gradually and applying global damping to dissipate kinetic energy. For the global damping, a damping force  $\mathbf{F}^{\text{GD}}$ , which is proportional to the absolute velocity of a

sphere, is exerted on the sphere in the direction opposite to the sphere velocity  $\mathbf{v}_s$ , i.e.,  $\mathbf{F}^{\text{GD}} = -C^{\text{GD}} \mathbf{v}_s$ , in which the damping coefficient  $C^{\text{GD}}$  is taken to be proportional to the mass of sphere, i.e.,  $C^{\text{GD}} = \alpha m_s$ . The normalized deflection of the center of the sphere at the free end of cantilever,  $y^0/(L - r_s)$ , is plotted in Fig. 3a as a function of the normalized loading,  $F_t^0(L - r_s)^2/(EI)$ , in which  $y^0$  represents the deflection of the center of the sphere at the free end of cantilever,  $L$  is the length of the cantilever,  $r_s$  is the radius of the constituent sphere, and  $F_t^0$  is the applied shear force (see Fig. 2). In Fig. 3a, the simulation results with four different fiber models formed by bonding 4, 6, 10, and 12 spheres, respectively, are compared with small bending deformation theory (also known as Euler–Bernoulli beam theory) and large bending deformation theory [16] for thin beams. The errors of the simulation results from the large deformation theory are shown in Fig. 3b. It can be seen that the simulation results are in good agreement with both small and large deformation theories when the deflection is small ( $|y^0/(L - r_s)| < 0.2$ ), with the errors generally less than 2% (Fig. 3b). When large deflection occurs ( $|y^0/(L - r_s)| > 0.2$ ), the simulation results with various fiber models are better predicted by the large deformation theory (Fig. 3a). As the number of spheres in a fiber decreases, the departure from the large deformation theory increases. As shown in Fig. 3b, the simulation errors are below 4% for the models with sphere numbers greater than and equal to 6, but the error can exceed 6% for the 4-sphere fiber model at large deflections. Hence, the number of spheres in a fiber is set to 10 in the simulations presented in the following paragraphs.

According to the small bending deformation theory, the distributions of shear force  $F_t$ , bending moment  $M$ , and deflection  $y$  along the  $x$ -axis follow,

$$F_t(x) = F_t^0 \text{ and } F_t^{\text{max}} = F_t^0, \quad (7)$$

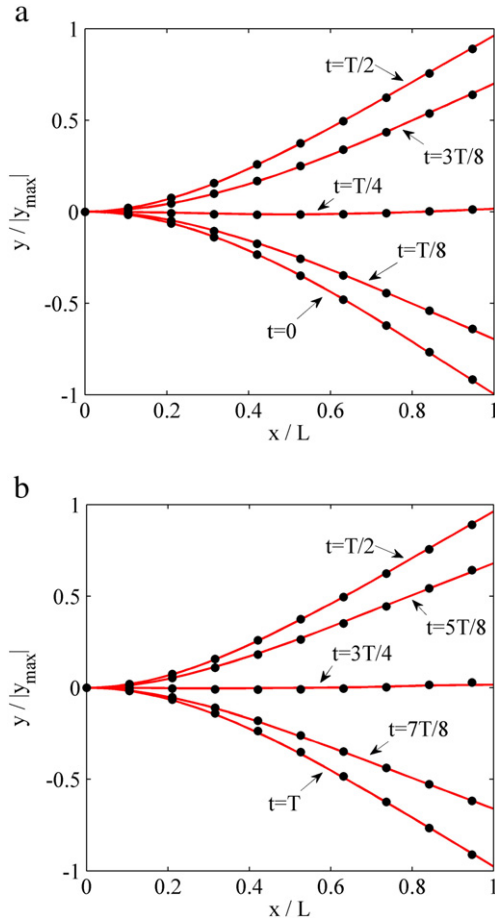


Fig. 5. Transient deflection profiles at various time instants in the first half (a) and second half (b) of a period during fiber bending vibration. (Curves represent analytical solutions and dots represent DEM results.)

$$M(x) = F_t^0(L - r_s - x) \text{ and } M_{\max} = F_t^0(L - r_s), \quad (8)$$

$$y(x) = \begin{cases} -\frac{F_t^0 x^2 (3L - 3r_s - x)}{6EI} & 0 \leq x \leq L - r_s \\ -\frac{F_t^0 (L - r_s)^2 (3x - L + r_s)}{6EI} & L - r_s < x \leq L \end{cases} \text{ and } y_{\max} = -\frac{F_t^0 (L - r_s)^2 (2L + r_s)}{6EI}, \quad (9)$$

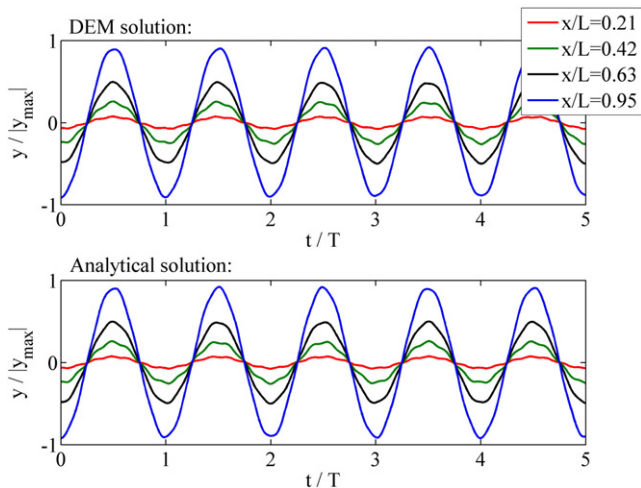


Fig. 6. Time evolution of the scaled deflections at various positions in a fiber during bending vibration.

in which  $F_t^{\max}$ ,  $M_{\max}$  and  $y_{\max}$  are the maximum magnitudes. The DEM results of cantilever bending with the deflection  $|y^0/(L - r_s)| = 0.15$  are compared with analytical solutions (based on Eqs. (7)–(9)) in Fig. 4. Good agreement is obtained with maximum errors of 2.9% for the shear force  $F_t$ , 1.2% for the bending moment  $M$ , and 1.8% for the deflection  $y$ .

After releasing the load  $F_t^0$ , the fiber exhibits free vibration in the absence of gravity and global damping. The governing equation for the free vibration of a fiber with small bending deformation ( $|y^0/(L - r_s)| \leq 0.2$ ) can be written as,

$$EI \frac{\partial^4 y(x, t)}{\partial x^4} = -\rho_l \frac{\partial^2 y(x, t)}{\partial t^2}, \quad (10)$$

in which  $\rho_l$  is the mass per unit length of the beam and  $t$  represents time. By separating variables and applying the boundary conditions ( $y(0, t) = 0$ ,  $\partial y(0, t)/\partial x = 0$ ,  $\partial^2 y(L, t)/\partial x^2 = 0$ , and  $\partial^3 y(L, t)/\partial x^3 = 0$ ), Eq. (10) can be solved to give,

$$y(x, t) = \sum_{n=1}^{+\infty} A_n Y_n(x) \cos(\omega_n t), \quad (11)$$

in which,

$$Y_n(x) = 0.5 \left\{ \frac{[\cos(k_n x) - \cosh(k_n x)] - [\cos(k_n L) + \cosh(k_n L)] [\sin(k_n x) - \sinh(k_n x)]}{\sin(k_n L) + \sinh(k_n L)} \right\}, \quad (12)$$

$$A_n = \frac{\int_0^L y(x, t=0) Y_n(x) dx}{\int_0^L Y_n^2(x) dx}, \quad (13)$$

$$\omega_n = k_n^2 \sqrt{\frac{EI}{\rho_l}}, \quad (14)$$

with  $k_n$  satisfying,

$$\cos(k_n L) \cosh(k_n L) = -1. \quad (15)$$

The solutions for the first four modes are,

$$k_1 L = 1.8752, k_2 L = 4.6941, k_3 L = 7.8548, k_4 L = 10.996. \quad (16)$$

In Eq. (13), the initial configuration of the beam,  $y(x, t = 0)$ , can be obtained from Eq. (9). The period of vibration can be evaluated based on the natural frequency of the first mode, which dominates the vibration, i.e.,

$$T = \frac{2\pi}{\omega_1} = 1.7868 \cdot L^2 \sqrt{\frac{\rho_l}{EI}}. \quad (17)$$

The transient profiles of the normalized deflection,  $y/|y_{\max}|$ , at various time instants within a period  $T$  are shown in Fig. 5, in which the curves represent analytical solutions based on Eqs. (10)–(17) and the dots represent the DEM simulation results. The time evolution of the normalized deflections at various positions of a fiber is shown in Fig. 6. Good agreement is also obtained between the DEM results and analytical solutions. The maximum error of the simulation from the theoretical prediction is 4.3%.

#### 4. Fiber stretching/compressing

The axial deformation of a fiber under static load  $F_n^0$  is simulated as shown in Fig. 7. The global damping is applied to dissipate the kinetic energy to achieve the static equilibrium state. The distributions along



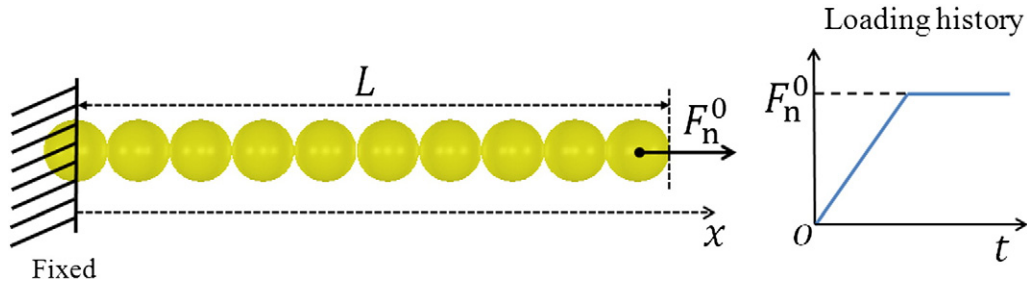


Fig. 7. Axial extension/compression of a fiber.

the x-axis of normal force  $F_n$  and normal displacement  $\delta_n$  (defined as  $\delta_n = x(t) - x(0)$ , in which  $x(t)$  is the current x-position and  $x(0)$  is the initial x-position of a cross section perpendicular to the x-axis) are given by,

$$F_n(x) = F_n^0 \text{ and } F_n^{\max} = F_n^0, \quad (18)$$

$$\delta_n(x) = \begin{cases} \frac{F_n^0}{EA}x & 0 \leq x \leq L - r_s \\ \frac{F_n^0}{EA}(L - r_s) & L - r_s \leq x \leq L \end{cases} \text{ and } \delta_n^{\max} = \frac{F_n^0}{EA}(L - r_s), \quad (19)$$

in which  $F_n^{\max}$  and  $\delta_n^{\max}$  are the maximum magnitudes. The results obtained from DEM simulations are compared with the analytical solutions (Eqs. (18) and (19)), as shown in Fig. 8. Excellent agreement is achieved with maximum errors of 0.012% for the normal force  $F_n$  and 0.0051% for the normal displacement  $\delta_n$ .

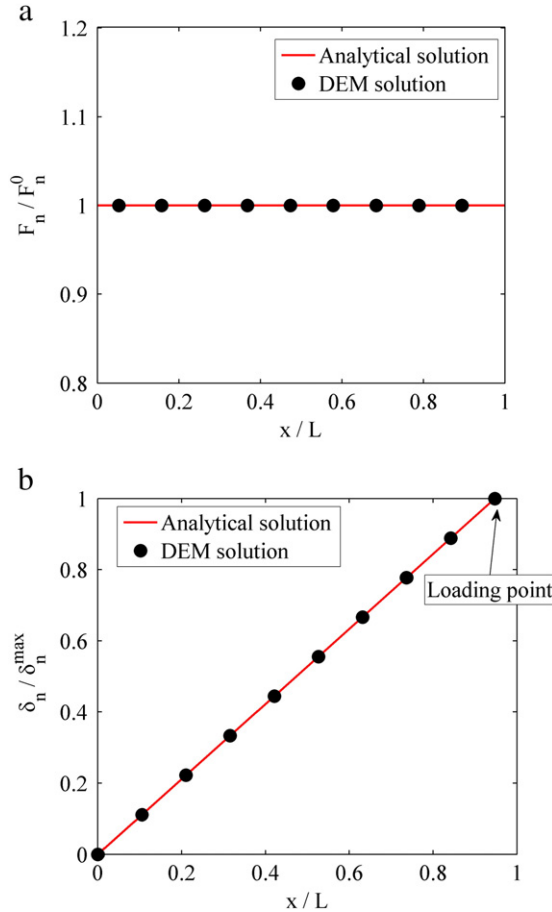


Fig. 8. Distributions of normal force (a) and normal displacement (b) in case of fiber extension/compression.

The sudden release of the normal force leads to axial vibration in the absence of global damping, which is modeled by,

$$EA \frac{\partial^2 \delta_n(x, t)}{\partial x^2} = \rho_l \frac{\partial^2 \delta_n(x, t)}{\partial t^2}. \quad (20)$$

By applying the boundary conditions ( $\delta_n(0, t) = 0$  and  $\partial \delta_n(L, t) / \partial x = 0$ ), Eq. (20) has the solution,

$$\delta_n(x, t) = \sum_{n=1}^{+\infty} B_n \sin(k^{\text{axi}} \omega_n^{\text{axi}} x) \cos(\omega_n^{\text{axi}} t), \quad (21)$$

in which

$$B_n = \frac{2F_n^0 L}{EA} \cdot \frac{\sin(n-0.5)\pi}{(n-0.5)^2 \pi^2}, \quad (22)$$

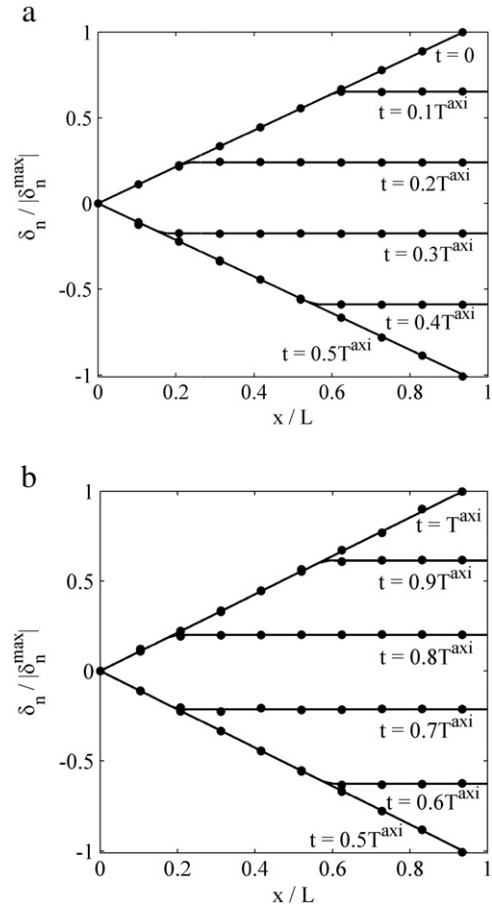


Fig. 9. Transient normal displacement profiles at various time instants in the first half (a) and second half (b) of a period during the axial vibration. (Curves represent analytical solutions and dots represent DEM results.)

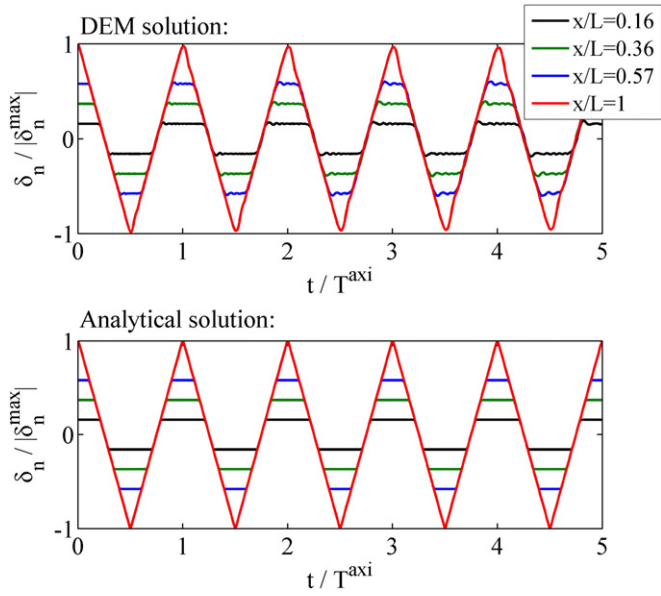


Fig. 10. Time evolution of the scaled normal displacement at various positions in a fiber during the axial vibration.

$$k^{\text{axi}} = \sqrt{\frac{\rho_l}{EA}}, \quad (23)$$

and,

$$\omega_n^{\text{axi}} = \frac{(n-0.5)\pi}{k^{\text{axi}}L}. \quad (24)$$

The period of the vibration can be evaluated based on the natural frequency of the first mode as,

$$T^{\text{axi}} = \frac{2\pi}{\omega_1^{\text{axi}}} = 4L\sqrt{\frac{\rho_l}{EA}}. \quad (25)$$

Good agreement was obtained with a maximum error of 5.3% between the DEM results and the analytical solutions (Eqs. (20)–(25)) for the transient normal displacement profiles at various time instants in a period as shown in Fig. 9 and for the time evolution of the normal displacements at various positions in the fiber as shown in Fig. 10.

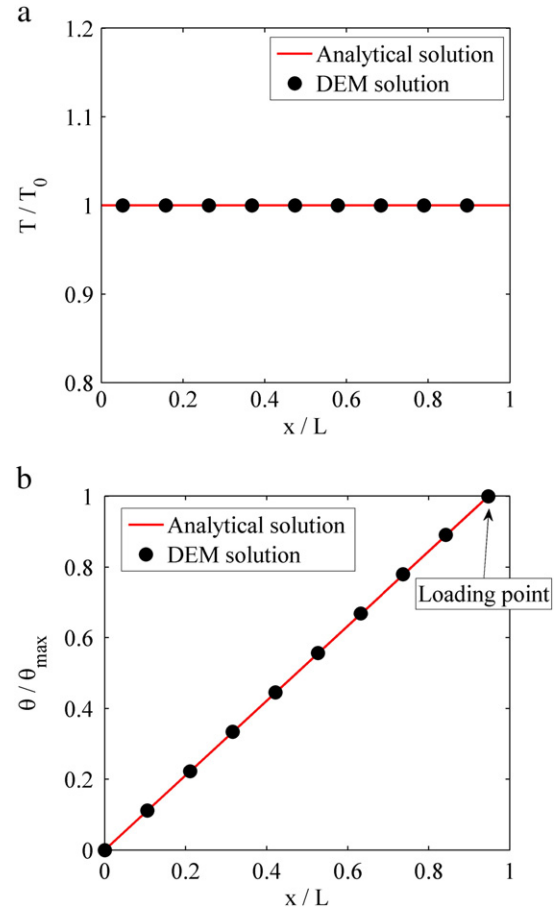


Fig. 12. Distributions of torque (a) and angular displacement (b) in case of fiber torsional deformation.

## 5. Fiber twisting

A fiber may also experience torsional deformation under an axial torque, as shown in Fig. 11. The governing equations for fiber twisting, which are similar to those for fiber stretching, can be obtained by replacing  $F_n$ ,  $F_n^0$ ,  $\delta_n$ ,  $EA$ , and  $\rho_l$  in Eqs. (18)–(20) with  $T$ ,  $T^0$ ,  $\theta$ ,  $GI_p$ , and  $J_l$ , respectively, in which  $T$  represents the torque distribution,  $T^0$  is the applied torque,  $\theta$  is the torsional angle, and  $J_l$  is the moment of inertia per unit length of a fiber. Thus, the period of the torsional vibration can be expressed as  $T^{\text{tor}} = 4L\sqrt{\frac{J_l}{GIp}}$ . The distributions of torque and angular

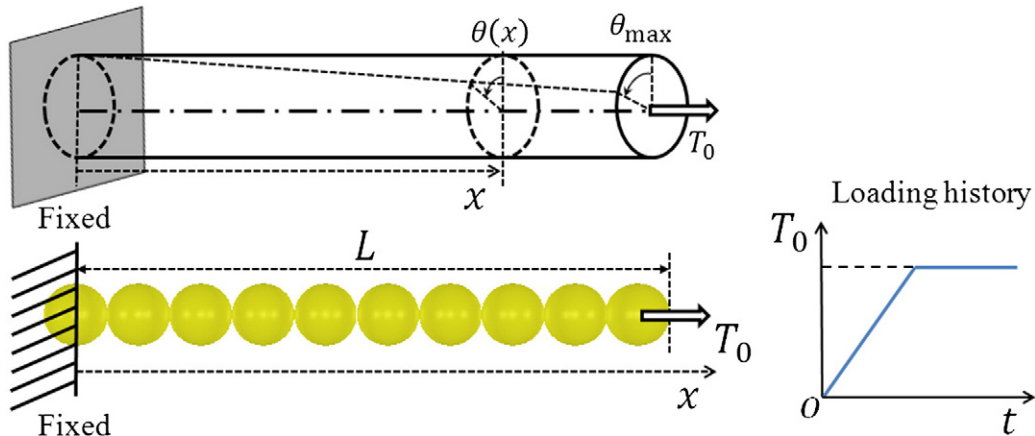
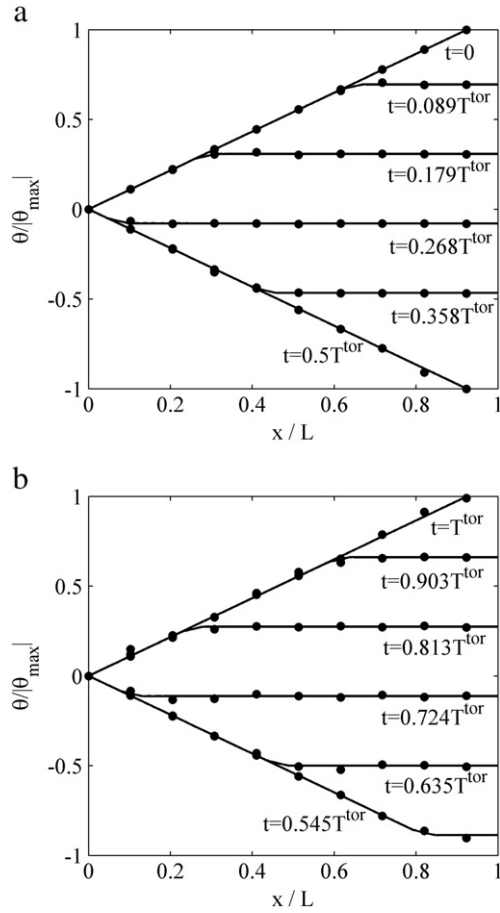
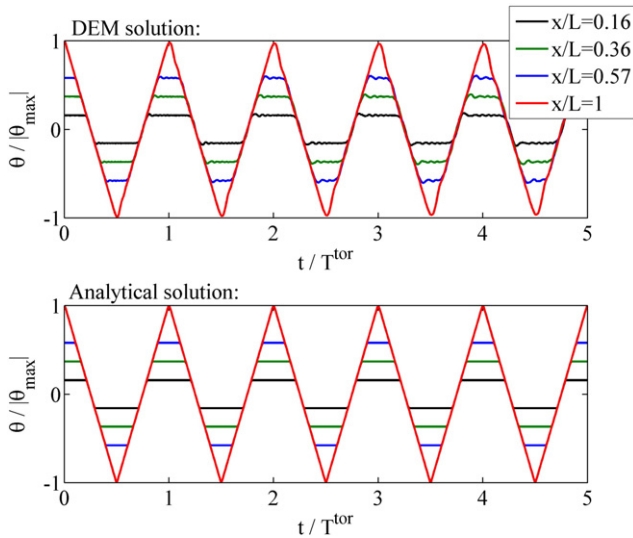


Fig. 11. Torsional deformation of a fiber.



**Fig. 13.** Transient angular displacement profiles at various time instants in the first half (a) and second half (b) of a period during fiber torsional vibration. (Curves represent the analytical solutions and dots represent the DEM results.)

displacement under the static loading are shown in Fig. 12. The maximum errors of the DEM simulations compared to the analytical solutions are 0.01% for the torque  $T$  and 0.29% for the angular displacement  $\theta$ . For the torsional vibration, the transient angular displacement profiles at various time instants in a period of vibration are shown in Fig. 13, and the time evolutions of the angular displacement at various positions in



**Fig. 14.** Time evolution of the scaled angular displacement at various positions in a fiber during fiber torsional vibration.

a fiber are shown in Fig. 14. The maximum error of the simulation results from the analytical solutions is 4.7%.

## 6. Time step

In the DEM modeling of dynamic vibrations of a fiber, the elastic waves should not travel longer than a single bond length within a time step. Therefore, the largest time step should be determined by the largest wave speed in order to capture the correct propagation behavior for all types of elastic waves.

According to Eqs. (12) and (14), the speed of the bending wave,  $v_{\text{bend}}$ , that propagates through an elastic beam can be estimated based on the first mode of vibration as,

$$v_{\text{bend}} = \frac{\omega_1}{k_1} = k_1 \sqrt{\frac{EI}{\rho_l}} = \frac{1.8752}{L} \sqrt{\frac{EI}{\rho_l}}. \quad (26)$$

Therefore, the time,  $\Delta t_{\text{bend}}$ , required for the bending wave to travel through a single bond of length  $l_b$  is,

$$\Delta t_{\text{bend}} = \frac{l_b}{v_{\text{bend}}} = \frac{L \cdot l_b}{1.8752} \sqrt{\frac{\rho_l}{EI}}. \quad (27)$$

The mass per unit length of a bonded-spheres fiber in DEM modeling is given by,

$$\rho_l = \frac{\rho_m \frac{1}{6} \pi d_s^3}{d_s} = \frac{1}{6} \pi \rho_m d_s^2, \quad (28)$$

in which  $\rho_m$  is the material density of the spheres in a fiber and  $d_s$  is the diameter of the spheres.

In DEM modeling, it is assumed that the radius of the cylindrical bonds  $r_b$  is equal to the radius of the spheres  $r_s$ , therefore,

$$I = \frac{\pi r_b^4}{4} = \frac{\pi r_s^4}{4} = \frac{\pi d_s^4}{64}. \quad (29)$$

Substituting Eqs. (28) and (29) into Eq. (27) gives,

$$\Delta t_{\text{bend}} = 1.7417 \cdot \frac{L}{d_s} \cdot l_b \sqrt{\frac{\rho_m}{E}}. \quad (30)$$

Similarly, the wave speed for the axial extensional/compressional vibration,  $v_{\text{axi}}$ , and the time,  $\Delta t_{\text{axi}}$ , required for this wave to travel through a single bond of length  $l_b$  can be obtained as,

$$v_{\text{axi}} = \frac{1}{k^{\text{axi}}} = \sqrt{\frac{EA}{\rho_l}}, \quad (31)$$

and,

$$\Delta t_{\text{axi}} = l_b \sqrt{\frac{\rho_l}{EA}} = 0.8165 \cdot l_b \sqrt{\frac{\rho_m}{E}}. \quad (32)$$

Also, the wave speed for the torsional vibration,  $v_{\text{tor}}$ , and the time,  $\Delta t_{\text{tor}}$ , required for this wave to travel through a single bond of length  $l_b$  are,

$$v_{\text{tor}} = \frac{1}{k^{\text{tor}}} = \sqrt{\frac{GI_p}{J_l}}, \quad (33)$$

and,

$$\Delta t_{\text{tor}} = l_b \sqrt{\frac{J_l}{GI_p}}, \quad (34)$$



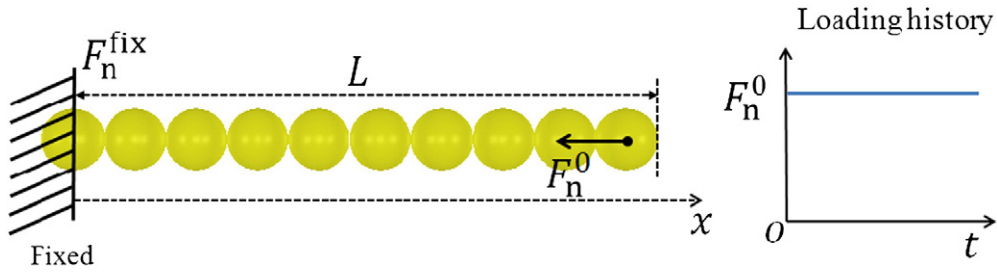


Fig. 15. Axial vibration of a fiber driven by a constant compressive force  $F_n^0$  applied to the free end.

in which,

$$J_l = \frac{J_s}{d_s} = \frac{\pi}{60} \rho_m d_s^4, \quad (35)$$

and,

$$I_p = \frac{\pi d_s^4}{32}. \quad (36)$$

Substituting Eqs. (35), (36), and  $G = \frac{E}{2(1+\xi)}$  into Eq. (34) gives,

$$\Delta t_{\text{tor}} = \sqrt{\frac{16(1+\xi)}{15}} \cdot l_b \sqrt{\frac{\rho_m}{E}}. \quad (37)$$

In the DEM modeling of an assembly of spheres, to account for surface elastic wave propagation, a Rayleigh wave cannot pass a sphere within a single time step [17,18], leading to the critical time step for the sphere–sphere contact,  $\Delta t_{\text{con}}$ , as,

$$v_{\text{Ray}} = \lambda \sqrt{\frac{G}{\rho_m}}, \quad (38)$$

$$\lambda = 0.1631\xi + 0.8766, \quad (39)$$

and,

$$\Delta t_{\text{con}} = \frac{0.5\pi d_s}{v_{\text{Ray}}} = \frac{\pi d_s}{2\lambda} \sqrt{\frac{\rho_m}{G}} = \frac{\pi}{\lambda} \sqrt{\frac{1+\xi}{2}} \cdot d_s \sqrt{\frac{\rho_m}{E}}, \quad (40)$$

in which  $v_{\text{Ray}}$  is the speed of the Rayleigh wave.

The time step in the modeling of fibers using the present model should be determined by the minimum value of these four critical time durations:  $\Delta t_{\text{bend}}$ ,  $\Delta t_{\text{axi}}$ ,  $\Delta t_{\text{tor}}$ , and  $\Delta t_{\text{con}}$ . It is found that  $\Delta t_{\text{axi}}$  is the minimum by comparing Eqs. (30), (32), (37), and (40). Therefore, the time step  $\Delta t$  in the DEM algorithm should be determined by axial wave propagation, i.e.,

$$\Delta t < \Delta t_{\text{axi}} = 0.8165 \cdot l_b \sqrt{\frac{\rho_m}{E}}. \quad (41)$$

To verify this time step criterion (Eq. (41)), the axial vibration of a fiber, driven by a compressive force  $F_n^0$ , is simulated as shown in Fig. 15. The compressive force  $F_n^0$  is suddenly applied to the free end of the fiber at the beginning of vibration and remains constant throughout the process. The expected travel time,  $t_{\text{exp}}$ , for the force  $F_n^0$  to transmit from the free end to the fixed end is,

$$t_{\text{exp}} = \frac{L}{v_{\text{axi}}} = L \sqrt{\frac{\rho_l}{EA}} = 0.25 T^{\text{axi}}, \quad (42)$$

in which  $T^{\text{axi}}$  is the period given by Eq. (25). The evolution of the normal force acting on the fixed end,  $F_n^{\text{fix}}$ , with various time steps are shown in Fig. 16, in which  $\Delta t_{\text{axi}}$  is the critical time step given by Eq. (41). It can be seen from Fig. 16a, the normal force at the fixed end  $F_n^{\text{fix}}$  is abruptly increased to the applied force  $F_n^0$  (i.e.,  $\frac{F_n^{\text{fix}}}{F_n^0} = 1$ ) at the time instant  $t = 0.25 T^{\text{axi}}$  (i.e.,  $\frac{t}{T^{\text{axi}}} = 0.25$ ), and reaches  $2F_n^0$  (i.e.,  $\frac{F_n^{\text{fix}}}{F_n^0} \approx 2$ ) shortly after  $t = 0.25 T^{\text{axi}}$ . Thus, the DEM simulations predict that the time for the force  $F_n^0$  transmitting from the free end to the fixed end is equal to the expected travel time  $t_{\text{exp}}$  given by Eq. (42). Using time steps less than  $\Delta t_{\text{axi}}$  (i.e.,  $\frac{\Delta t_{\text{axi}}}{16}$ ,  $\frac{\Delta t_{\text{axi}}}{8}$ ,  $\frac{\Delta t_{\text{axi}}}{4}$ , and  $\frac{\Delta t_{\text{axi}}}{2}$ ) provides nearly the same results. However, if the time step is set to  $\Delta t_{\text{axi}}$  exactly, the same force transmission time is obtained, but the force fluctuations at the ends of loading and unloading are reduced. These force fluctuations, which were also observed in the

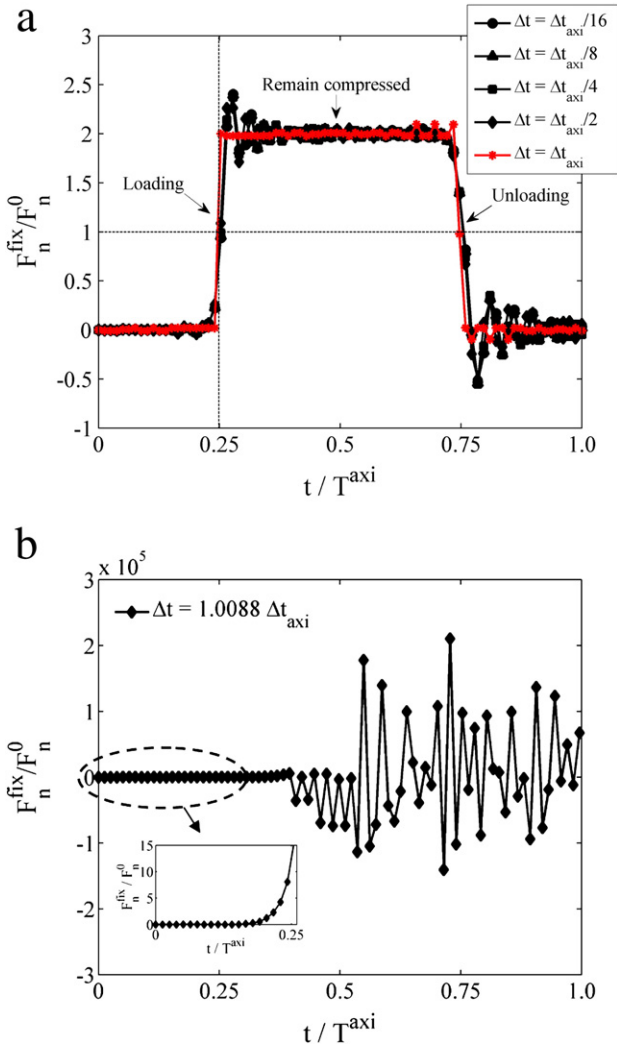


Fig. 16. Simulated time evolution of the normal force  $F_n^{\text{fix}}$  at the fixed end of the fiber with the time steps  $\Delta t \leq \Delta t_{\text{axi}}$  (a) and  $\Delta t > \Delta t_{\text{axi}}$  (b).

longitudinal vibration of a continuum beam excited by impulse loading [19], represent the higher modes of vibration rather than numerical artifacts. In addition, the fluctuations may be relevant to the Gibbs phenomenon. In mathematics, the Gibbs phenomenon is the peculiar manner in which the  $n$ th partial sum of the Fourier series of a piecewise continuously differentiable periodic function has large oscillations at a jump discontinuity. In the present simulations, the sudden application of the force  $F_n^0$  (Fig. 15) at the initial time of  $t = 0$ , which is similar to a Heaviside step function impulse, leads to oscillations near the force jumps.

Interestingly, if the time step  $\Delta t$  is slightly greater than  $\Delta t_{\text{axi}}$  (i.e.,  $\Delta t = 1.0088 \Delta t_{\text{axi}}$ ), as shown in Fig. 16b, the simulation eventually diverges. It is also found that the divergence occurs earlier with a larger time step  $\Delta t = 1.1 \Delta t_{\text{axi}}$  (not shown here). Hence, it is evident that the criterion given by Eq. (41) should be used to determine the time step for the DEM modeling of fibers that are formed by bonding spheres.

## 7. Conclusion

A comprehensive approach is taken to verify a flexible fiber model based on the Discrete Element Method and the bonded-particle model by Potyondy and Cundall [13]. In the verification, the static and dynamic behavior of fiber bending, stretching/compressing, and twisting is modeled and compared with theoretical predictions. It is found that the accuracy of numerical modeling decreases as the number of spheres in a fiber decreases. The errors of the bending deflections from the small deformation theory (when  $|y^0/(L - r_s)| < 0.2$ ) and the large deformation theory (when  $|y^0/(L - r_s)| > 0.2$ ) are less than 5% when the number of spheres in a fiber is greater than or equal to six. To ensure numerical stability and capture correct dynamic behavior of fibers, the time that it takes for the axial extensional/compression wave to travel a single bond length should be used as the upper limit for the time step.

## Acknowledgements

This research is supported by funding from NSF-CBET Grant No. 0854005, the State of Florida Space Research Initiative, and the Shell Oil Company. The authors also acknowledge the University of Florida High-Performance Computing Center for providing computational resources.

## References

- [1] S. Yamamoto, T. Matsuoka, A method for dynamic simulation of rigid and flexible fibers in a flow field, *J. Chem. Phys.* 98 (1993) 644–650.
- [2] K.K. Kabanemi, J.-F. Hétu, Effects of bending and torsion rigidity on deformation and breakage of flexible fibers: a direct simulation study, *J. Chem. Phys.* 136 (2012) 074903.
- [3] J. Park, N. Kang, Applications of fiber models based on discrete element method to string vibration, *J. Mech. Sci. Technol.* 23 (2009) 372–380.
- [4] D.H. Nguyen, N. Kang, J. Park, Validation of partially flexible rod model based on discrete element method using beam deflection and vibration, *Powder Technol.* 237 (2013) 147–152.
- [5] R.F. Ross, D.J. Klingenberg, Dynamic simulation of flexible fibers composed of linked rigid bodies, *J. Chem. Phys.* 106 (1997) 2949–2960.
- [6] Z. Ning, J.R. Melrose, A numerical model for simulating mechanical behavior of flexible fibers, *J. Chem. Phys.* 111 (1999) 10717–10726.
- [7] F. Geng, Y. Li, X. Wang, Z. Yuan, Y. Yan, D. Luo, Simulation of dynamic processes on flexible filamentous particles in the transverse section of a rotary dryer and its comparison with video-imaging experiments, *Powder Technol.* 207 (2011) 175–182.
- [8] J. Wu, C.K. Aidun, A method for direct simulation of flexible fiber suspensions using lattice Boltzmann equation with external boundary force, *Int. J. Multiphase Flow* 36 (2010) 202–209.
- [9] S.B. Lindstrom, T. Uesaka, Simulation of the motion of flexible fibers in viscous fluid flow, *Phys. Fluids* 19 (2007) 113307.
- [10] G. Wang, W. Yu, C. Zhou, Optimization of the rod chain model to simulate the motions of a long flexible fiber in simple shear flows, *Eur. J. Mech. B. Fluids* 25 (2006) 337–347.
- [11] D. Qi, A new method for direct simulations of flexible filament suspensions in non-zero Reynolds number flows, *Int. J. Numer. Methods Fluids* 54 (2007) 103–118.
- [12] A. Biswas, H. Park, W.M. Sigmund, Flexible ceramic nanofiber mats electrospun from  $\text{TiO}_2$ - $\text{SiO}_2$  aqueous sol, *Ceram. Int.* 38 (2012) 883–886.
- [13] D.O. Potyondy, P.A. Cundall, A bonded-particle model for rock, *Int. J. Rock Mech. Min. Sci.* 41 (2004) 1329–1364.
- [14] C.J. Coetzee, S.G. Lombard, The destemming of grapes: experiments and discrete element modelling, *Biosyst. Eng.* 114 (2013) 232–248.
- [15] C. Thornton, K.K. Yin, Impact of elastic spheres with and without adhesion, *Powder Technol.* 65 (1991) 153–165.
- [16] J.M. Gere, S.P. Timoshenko, *Mechanics of Materials*, 2nd ed. Van Nostrand, Reinhold, London, 1987.
- [17] C. Thornton, W. Randall, Applications of theoretical contact mechanics to solid particle system simulation, in: M. Satake, J.T. Jenkins (Eds.), *Micromechanics of granular materials*, Elsevier, Amsterdam, 1988, pp. 133–142.
- [18] K.D. Kafui, C. Thornton, M.J. Adams, Discrete particle-continuum fluid modelling of gas–solid fluidised beds, *Chem. Eng. Sci.* 57 (2002) 2395–2410.
- [19] J. Fortgang, W. Singhose, Input shaping for continuum beams under longitudinal vibration, *Proceedings of the 2005 IEEE/ASME International Conference on Advanced Intelligent Mechatronics*, Monterey, California, USA, 24–28 July, 2005, 2005.